



# Achieving high strength and large ductility of an ultrafine-grained 211ZX aluminium alloy processed by improved thermomechanical processing

Tao Luo<sup>1</sup> · Lei Lei<sup>2,3</sup> · Ke Feng<sup>4</sup> · Ming Yang<sup>1</sup> · Yun Jiang<sup>5</sup>

Received: 11 December 2022 / Revised: 6 April 2023 / Accepted: 6 April 2023 / Published online: 25 April 2023  
© Wrocław University of Science and Technology 2023

## Abstract

Simultaneously achieving high strength and ductility has been a long-standing goal in aluminum alloys, while the increase in strength usually leads to ductility loss. In this study, a novel thermomechanical treatment (TMT) method, i.e., pre-existing precipitation in coarse grain (CG) and cryogenic rolling plus warm rolling followed by peak aging, is developed to achieve high strength and good ductility in 211ZX aluminum alloy. As a result, a composite nanostructure including ultrafine-grained (UFG) and nanoprecipitation is obtained. Compared to a conventional T6 sample, the multi-step TMT sample has a finer grain (205 nm), while numerous GP zones and  $\theta''$  phases are dispersed inside the grain. The precipitation characteristics are similar to the T6 sample. The yield strength (635 MPa) and ultimate tensile strength (690 MPa) are about 81% and 53% higher than the T6 sample, respectively, with only a slight decrease in plasticity. Microstructural characterization and thermodynamic analysis confirmed that pre-existing precipitates and cryogenic temperatures facilitate the formation of the composite nanostructure. Quantitatively strengthening calculations demonstrate that the high strength is attributed to the ultra-fine grain strengthening and precipitation strengthening, while the high plasticity is mainly due to the reduction of dislocation density caused by recovery and recrystallization during the aging process as well as the massive production of nano-GIPs (interior grain precipitates).

**Keywords** 211ZX aluminum alloy · Multi-step thermomechanical treatment · Ultrafine-grained microstructure · Precipitation behavior · Strength-ductility synergy

## 1 Introduction

2xxx aluminum alloy is widely used in aerospace, transportation, and other fields due to its low density, high strength, and good formability [1–3]. The high strength of 2xxx aluminum can be attributed to interior grain precipitates controlled by solution treatment and aging. Besides precipitation hardening, fine grain strengthening plays a very significant role in determining the mechanical properties of the alloy. Thus, severe plastic deformation have been developed to produce materials with ultra-fine grains, such as equal-channel angular process (ECAP) [4–6], high-pressure torsion (HPT) [7, 8], and more recently, dual rolls equal channel extrusion (DRECE) [9, 10].

However, bulk nanostructured materials have difficulty achieving simultaneous improvement of strength and ductility, as reported in the literature [11–15]. The low ductility of ultrafine-grained materials is due to their inability to accumulate dislocations [16]. Thus, some researchers

---

✉ Ming Yang  
myang5@gzu.edu.cn

✉ Yun Jiang  
j\_yun7907@163.com

<sup>1</sup> School of Materials and Metallurgy, College of Materials and Metallurgy, Guizhou University, Guiyang 550025, China

<sup>2</sup> State Key Laboratory of Solidification Processing, Northwestern Polytechnical University, Xi'an 710072, China

<sup>3</sup> School of Physics and Optoelectronic Engineering, Yangtze University, Jingzhou 434023, China

<sup>4</sup> School of Materials Science and Engineering, Beijing Institute of Technology, Beijing 110004, China

<sup>5</sup> School of Mechanical Engineering, Guizhou University, Guiyang 550025, China

have attempted to improve the ductility of NG materials by inducing nanoprecipitation in nanograin or ultrafine grain with the logic that dislocations are forced to accumulate while shearing or bypassing the nanoprecipitation, leading to strain hardening. Unfortunately, for precipitation-hardening aluminum alloy, severe plastic deformation increases the density of crystalline defects, such as particularly dislocations and non-equilibrium grain boundaries, altering the precipitation sequence, shape, dimensions, and number density of the second phase particles during aging, which affects the efficiency of precipitation hardening in aluminum alloys [17–19]. Recently, many scholars found that cryorolling and subsequent aging increased the strength, ductility, and corrosion resistance of the aluminum alloy [20, 21]. Moreover, some scholars pointed out that cryorolling followed by warm rolling can improve the precipitation kinetics and aging hardening. Mei et al. [22] have investigated the Al–Zn–Mg–Cu sheet and reported an increase in its strength through the combined treatment of warm rolling (WR) and cryorolling (CR). The increase in the strength of an alloy has been attributed to the formation of fine precipitates during warm rolling at 393 K, and the increase in ductility has been attributed to the formation of fine equiaxed grains and the recovery effect. In addition, some researchers concluded that the precipitation in the initial coarse grain microstructure could also alter the aging precipitation behavior and improve the mechanical properties of UFG materials. For instance, Xu et al. [23] reported a precipitate optimization method wherein a high density of grain interior precipitation (GIPs) was obtained inside the 2024 nanocrystalline aluminum alloy by the appropriate introduction of GIPs embryo (solute-rich structures) in the coarse grain counterparts before heavy-room temperature rolling and aging.

Currently, investigations on the combined process of cryogenic rolling (CR), warm rolling (WR), and heat treatment of 2xxx alloy are rarely reported, and the coupling influence factors and mechanism still need to be further explored. In this paper, pre-existing precipitates are introduced into the initial CG microstructure to architect the nuclear-embryo structure of the precipitation phase. The influences of CR, WR, and artificial aging on microstructure and mechanical properties are investigated, and the relationships among the process, microstructure, and performance are revealed. The results of this research can provide theoretical support for the thermomechanical treatment (TMT) process design of the 211ZX alloy.

## 2 Experimental investigation

A self-developed new high-strength and heat-resistant 211ZX aluminum alloy was used in this study. The alloy has high thermal stability due to the micro-alloying of Mn,

Zr, and rare earth metal elements. The chemical composition measured by the AS6 JAGUAR Fluorescence spectrometer was Al-6.21Cu-0.37Mn-0.057Zr-0.07Fe-0.12Si-0.051Ti-xRE (wt.%). The hot deformation behavior and fatigue properties of the alloy have been extensively studied in previous work [24–26].

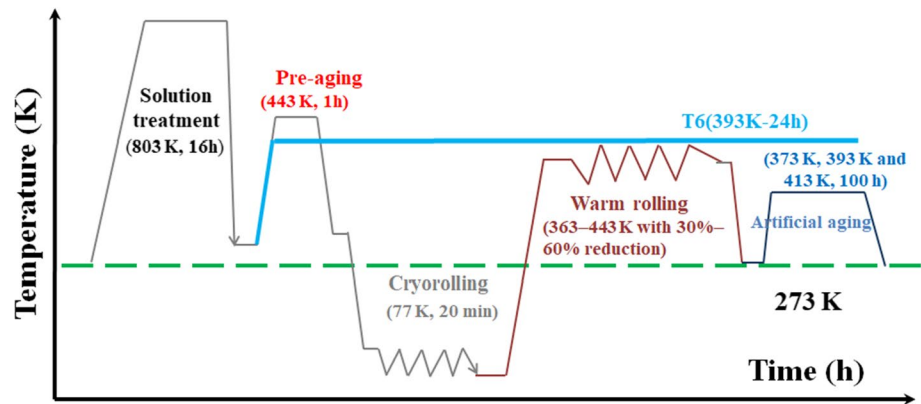
The sheet-shaped raw material with 10 mm thickness was made by melting, casting, rolling, and homogenizing processes. Next, the thick sheet was subjected to the multi-step TMT process. First, the sample was solution treated at 803 K for 16 h, followed by aging at 433 K for one hour. This sample was labeled as the UA sample throughout the manuscript. Next, the UA sample was cryogenically rolled, and the thickness reduction was 8% per pass. Before each rolling pass, the sheet was immersed in liquid nitrogen for at least 20 min to ensure the sheet was rolled at a temperature close to that of liquid nitrogen. Subsequently, the cryogenically rolled sample was warm rolled at 363 K–443 K with a 30%–60% reduction in a single pass. Lastly, the warm rolled sample was aged for 100 h at either 373 K, 393 K, or 413 K. For comparison, the peak-aging T6 sample was treated at 803 K for 16 h, followed by aging at 393 K for 24 h. A double roll mill with a diameter of 450 mm and a rolling speed of 20 rpm was used in the TMT process. A detailed summary of the sample identification and the corresponding process conditions is shown in Fig. 1.

The mechanical performance of the samples was characterized using Vickers microhardness and tensile testing. All samples were polished, and the hardness tests were performed on the samples at a load of 200 g and a dwell time of 10 s using an FM-800 micro-Vickers hardness tester. The reported values are the average of 10 indentations for each sample. For tensile testing, the rolled sheets were machined into dog-bone-shaped samples with a gauge length of 15 mm and a cross of 5 mm × 1 mm along the rolling direction. The tensile test was conducted on an MTS-810 tensile testing machine at room temperature, and the tensile rate was  $1 \times 10^{-3} \text{ s}^{-1}$ . The values of strength and ductility were taken from an average of three samples.

The longitudinal, transverse, and rolling sections of the sheets under different processing conditions were ground by SiC papers and then polished with Al<sub>2</sub>O<sub>3</sub> paste. The microstructure of the samples was observed using an OLYMPUS optical microscope after the sample was etched in Keller's reagent (1.5 mL HCl, 1 mL HF, 0.5 mL HNO<sub>3</sub>, and 95 mL distilled water). A SUPRA 40 scanning electron microscope (SEM) with a voltage of 20 kV was used to reveal the morphology of the tensile fracture of samples with different states.

Foils for transmission electron microscopy (TEM) observation were cut from the sample by wire electric discharge machine along the ND-RD cross-section and prepared by jet electropolishing in an electrolyte of 30% HNO<sub>3</sub> and

**Fig. 1** Experimental scheme of thermomechanical treatment (TMT) process



70% CH<sub>3</sub>OH at 298–303 K with an electrolysis voltage of 12–15 V and a current of 60–80 mA. The grain structure, dislocation morphologies, and precipitate characteristics of these samples were observed on FEI G2 F20 TEM equipped with a high-angle annular dark field (HAADF) detector.

X-ray diffraction (XRD) analysis was conducted on a PANalytical-Empyean X-ray diffractometer using Cu K $\alpha$  radiation (40 kV, 10 mA). Jade 6.0 software was used to analyze and calculate the XRD results to obtain dislocation density results [27, 28]. Three pole Figures (111), (200), and (220) were characterized with a PANalytical-Empyean X-ray diffractometer using the Schulz back-reflection method to measure the macro-textures of the various samples. Due to the inhomogeneity of the microstructure through-thickness of the alloy sheets during TMT processing, the texture

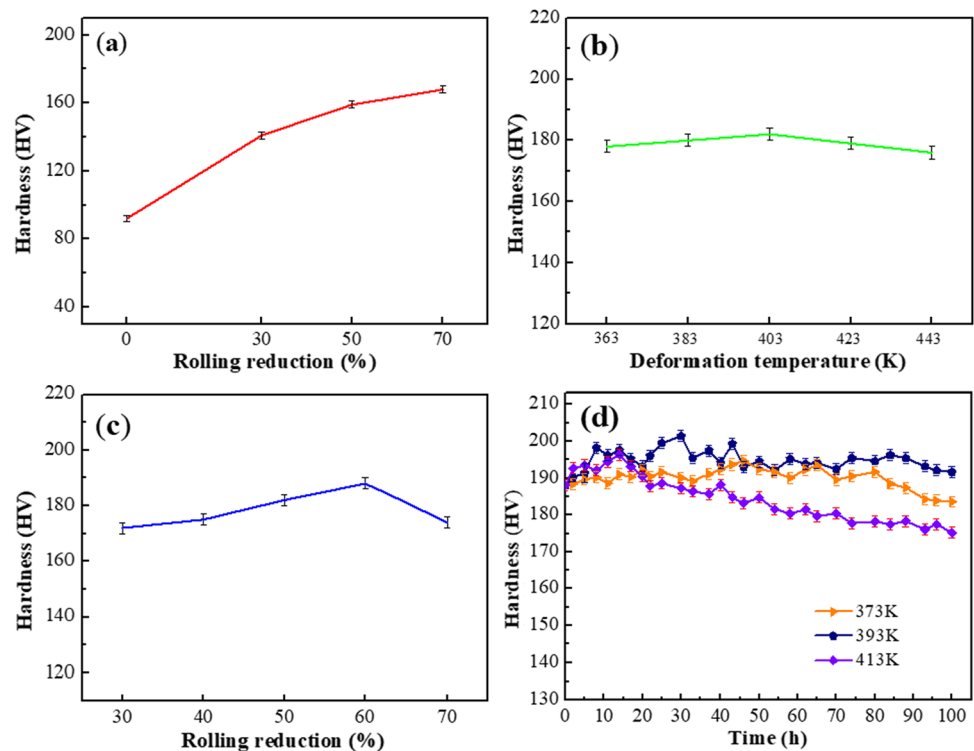
at one-fourth thickness of the sheet is commonly considered to be the average texture. The series expansion method was used to calculate the orientation distribution function (ODF) for each sample, and JETX software was used to draw the ODF map and calculate the volume fraction of texture.

## 3 Results

### 3.1 Mechanical properties

Figure 2a presents the effect of rolling reduction on the hardness of 211ZX alloy after CR. CR with reductions of 30%, 50%, and 70% increases the microhardness from 91 HV (after a solution treatment) to 143 HV, 159 HV, and 169

**Fig. 2** Hardness curves: **a** UA samples cryogenically rolled with different reductions; **b** CR samples warm rolled at different temperatures with 50% rolling reduction; **c** CR samples warm rolled at 403 K with different reductions; **d** WR samples aged for 100 h



HV, respectively. The UA sample with a reduction of 70% is defined as the CR sample. Figure 2b shows the variation in the hardness of CR samples subjected to warm rolling at different temperatures with a 50% reduction. The hardness first increases and then decreases. The maximum value is 183 HV when the rolling temperature is 403 K. The CR sample is subjected to different reductions at 403 K to further determine the appropriate reduction for warm rolling, and its changes in hardness are shown in Fig. 2c. It can be found that all CR samples show a similar trend with deformation temperature: hardness decreases after reaching its peak, and the maximum value is 188.5 HV when the rolling reduction is 60%. The hardness increment of the WR sample reflects the effectiveness of WR after CR in improving the mechanical properties. Thus, the CR sample warm rolled at 403 K with 60% rolling reduction is defined as the WR sample. In fact, the hardness increases with rolling strain due to the introduction of many dislocations and provides strain hardening. However, during the high temperature and larger rolling reduction, recovery and recrystallization occur, reducing the hardness of the alloys [12]. The WR samples are then aged successively at 373 K, 393 K, and 413 K for 100 h, and the hardness is shown in Fig. 2d. It can be seen that the hardness tends to increase first and then decrease with an increase in aging time. The trend is associated with hardening precipitation levels [14]. According to the hardness curve, the time taken to achieve peak hardness in the WR sample for 393 K is significantly reduced. Peak aging with a hardness of 201.4 HV is attained after 24 h at 393 K, which is defined as the WR-PA sample. A detailed summary of the sample identification is listed in Table 1.

The typical tensile stress–strain curves and mechanical properties values of 211ZX alloy at different processing states are shown in Fig. 3a and Table 2, respectively. According to Table 2, the T6 sample exhibits a relatively low yield strength (YS) of 350 MPa and ultimate tensile strength (UTS) of 450 MPa. On the other hand, the CR sample displays a higher yield strength (YS) of 510 MPa and ultimate tensile strength (UTS) of 549 MPa. After WR and aging, the yield strength and ultimate tensile strength reach up to

**Table 1** Sample identification and the corresponding processing condition

Sample	Processing
UA	Solution treated at 803 K for 16 h and aging at 433 K for one hour
CR	Cryogenically rolled UA sample with a reduction of 70%
WR	CR sample warm rolled at 403 K with 60% rolling reduction
WR-PA	WR sample aged at 393 K for 24 h
T6	Solution treated at 803 K for 16 h and aging at 393 K for 24 h

639 MPa and 690 MPa, respectively. The results indicate that TMT significantly improved the strength of the 211ZX alloy. The elongation of the CR specimen is only 5.3%, indicating that many dislocation multiplications occur during the CR process, depleting the strain-hardening ability [16]. However, the elongation of the WR-PA sample increased to 10.5%, suggesting that warm rolling and aging improve the ductility of the CR sample. The work hardening rate curves are shown in Fig. 3b. It can be seen that the work-hardening rates of the CR, WR, and WR-PA samples decrease rapidly with increasing rolling reduction, while the decline rate slowed down for these samples. The work hardening rate  $\left(\Theta = \frac{1}{\sigma} \left( \frac{\partial \sigma}{\partial \epsilon} \right) \dot{\epsilon} \right)$  reflects the plastic deformation ability of materials. Typically, when  $\Theta > 0$ , dislocations are further stored during deformation, and the materials are in a uniform deformation stage [29]. For the CR sample, the inflection point is located when the value of the true strain is 3.26%, while the inflection point is located when the value reaches 8.14% for the WR-PA sample. This result explains the higher ductility of the latter. Moreover, the WR-PA sample exhibits the highest product of strength and elongation of 7245 MPa%, which is 1.81, 1.53, and 1.33 times that of the T6 sample. Clearly, the WR-PA sample has the best strength-plastic synergy.

A careful examination of the fracture surface is made to reveal the mechanism involved in the fracture process.

**Fig. 3** **a** Tensile engineering stress–strain and **b** work hardening rate ( $\Theta$ ) curves of 211ZX aluminum alloy under different process conditions

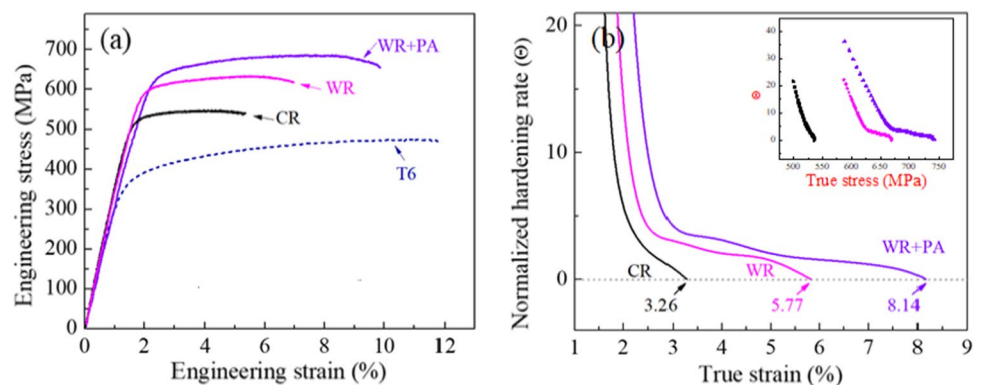




**Table 2** Mechanical properties of the tested samples

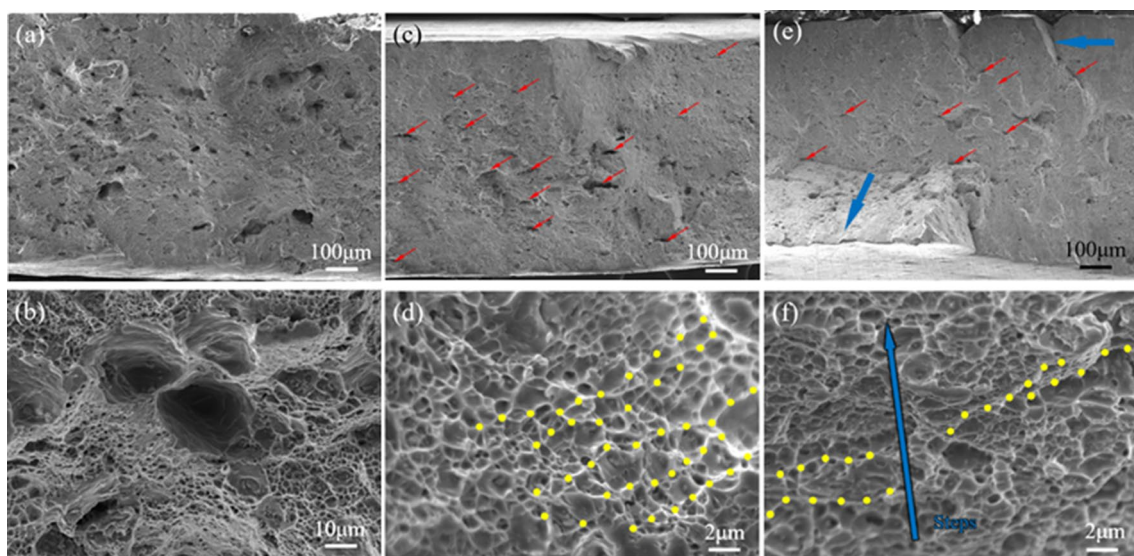
Sample	Ultimate tensile strength /MPa	Yield strength /MPa	Elongation /%	The product of the strength and elongation (PSE) (MPa·%)
T6	450	350	12.1	5445
CR	546	510	5.3	2893.8
WR	631	598	6.9	4353.9
WR-PA	690	635	10.5	7245

Figure 4a, c, e display the macroscopic fracture surfaces of the UA, WR, and WR-PA samples, while Figs. 4b, d, and f are the corresponding high-magnification images. The UA sample exhibits a typical ductile failure. Numerous dimples as large as several micrometers over the entire fracture surface are found at high magnification (Fig. 4b). After the fracture, the fracture surface of the WR sample is relatively smooth. WR sample displays micro-delaminations marked by the small (red) arrows in Fig. 4c. Similarly, the fracture surface of the WR-PA sample (Fig. 4e) also contains the characteristic of laminates. It is clear that the large dimples are replaced by fine dimples in the WR sample, resulting in a relatively low elongation. The same phenomenon was detected in the subsequent WR-PA sample, as shown in Fig. 4f. However, high-magnification images of the WR-PA sample reveal that such dimples are elongated rather than equiaxed, demonstrating that the more uniform plastic deformation occurs in the WR-PA sample [16]. Besides, comparing Fig. 4c with Fig. 4e, some shallow tear dimples are observed in the WR-PA sample, and a significant lamellae fracture formed by the junction of

small deep dimples is visible. This may be another reason for the higher elongation of the WR-PA sample [16].

### 3.2 Microstructural evolution

The microstructure evolution of the 211Z aluminum alloy after different processes was studied by TEM. Figure 5a displays that some spherical or rod-shaped particles with sizes of 100–500 nm are dispersed in the UA sample, which is verified as the T phase ( $\text{Al}_{20}\text{Cu}_2\text{Mn}_3$ ) by EDS analysis in the previous work conducted by the authors [30]. The distributed T-phase played a critical role in preventing grain growth [31]. In addition, many perpendicularly distributed needle-like precipitates are observed in Fig. 5b. High magnification TEM image indicated that the lengths of precipitates of the UA sample range from 10 to 20 nm, and the thickness is several nanometers (Fig. 5c). Their fast Fourier transform (FFT) diffractograms with simulated diffraction patterns are shown in Fig. 5d, e, f to identify these precipitates in the UA sample. In Fig. 5d, some continuous streaking appears along the  $\{020\}_{\text{Al}}$  direction, indicating that the corresponding precipitates are the GP zone [32]. The FFT diffractogram in Fig. 5e



**Fig. 4** Fracture morphology of samples with different states and different magnifications: **a, b** UA sample; **c, d** WR sample; **e, f** WR-PA sample

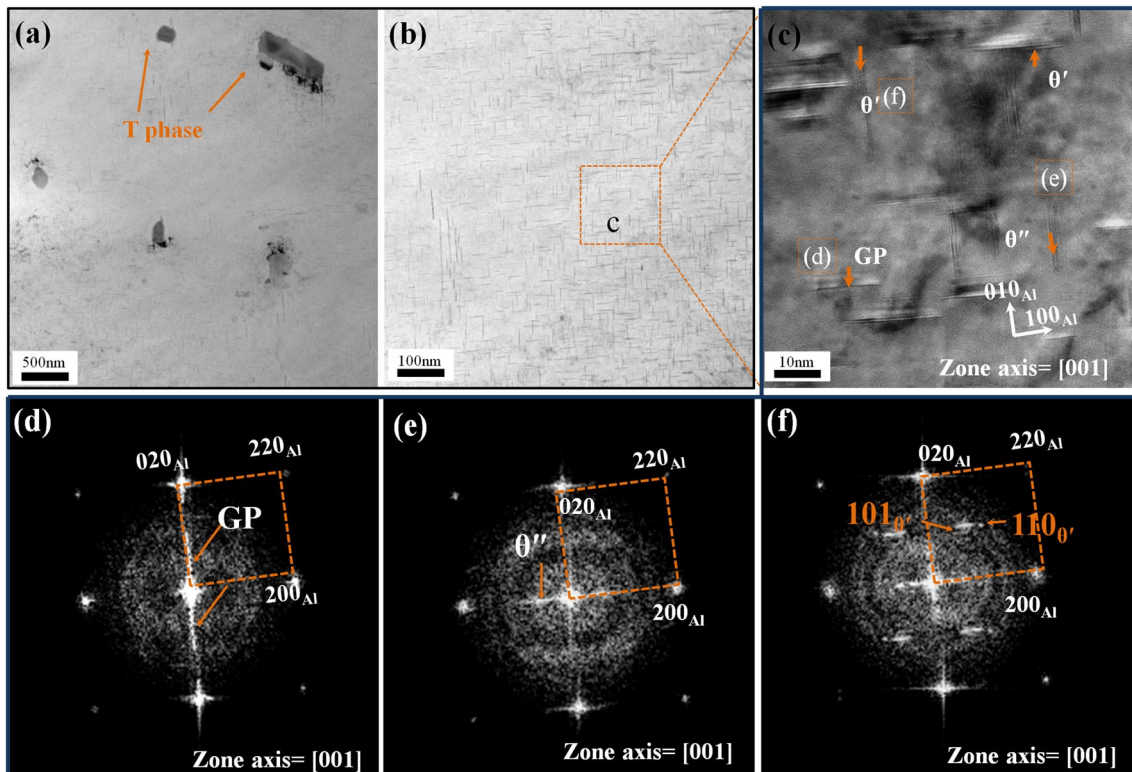


**Fig. 5** **a** T phase in the UA sample; **b** TEM micrograph of the UA sample; **c** high-resolution transmission electron microscopy (HRTEM) of the UA sample; **d–f** diffraction spots of GP Zone,  $\theta''$ , and  $\theta'$  phase in the UA sample after fast Fourier transform (FFT)

displays some continuous streaking along the  $\{200\}_{Al}$  direction, indicating that the corresponding precipitates are the  $\theta''$  phase [32]. Moreover, a bright spot at the  $\{110\}_{Al}$  can be seen in Fig. 5e. Such characteristic feature indicates that the precipitates are  $\theta'$  phase as reported in [33, 34].

Figures 6a, b show TEM bright-field images of the CR samples. It can be found that equiaxed grains and precipitates disappear in the matrix, and many dislocation cells and dislocation bands are observed in the matrix. These results indicate that the precipitates are completely redissolved after a 70% rolling reduction. Figures 6c–e are the TEM images of the WR samples. As shown in Fig. 6c, high densities of dislocations were trapped around the T-phase particles. However, the dislocation density is much lower in the area without T-phase particles. Different dislocation density indicates that the remaining T-phase plays an important role in dislocation accumulation during the CR process [31]. Meanwhile, the dislocation cells increase in size to about 500–600 nm in Fig. 6d. A sub-grain was observed in the high-magnification image of Fig. 6d1. The corresponding diffraction spots in Fig. 6d2 demonstrate short arc diffraction spots, suggesting that sub-grain structures with small misorientation were formed during WR [35]. However, there are no obvious precipitates in HRTEM imaging (Fig. 6f), and the corresponding diffraction spots also prove the result.

Therefore, it can be concluded that precipitates cannot form in the WR process. This result can be further confirmed by the XRD analysis shown in Fig. 9.

Figure 7 displays TEM images of the WR-PA sample. The dislocation cell in the sample has been transformed into equiaxed grains with an average size of 205 nm (Fig. 7b). The equiaxed grains have flat and straight boundaries, indicating that boundaries are formed with larger misorientation (Fig. 7c). Xu et al. pointed out that the form of misorientation originated due to dislocation multiplication, rearrangement, and dislocation reaction. Meanwhile, some other equiaxed grains have blurred interfaces, showing that mostly loose dislocation structures exist in grain boundaries. The corresponding diffraction spots consist of continuous rings, indicating a significant grain refinement (Fig. 7d) [35]. Furthermore, the bright field image (Fig. 7e) and high-angle annular dark-field scanning transmission electron microscopy (HAADF-STEM) image (Fig. 7f) display that the many needle-shaped precipitates are uniformly distributed in the grain interiors viewed along  $\langle 011 \rangle_{Al}$  (Fig. 7e). The presence of dispersed precipitates can be attributed to the nucleation and growth during the aging treatment. Additional inspection shows that these precipitates primarily grow along the  $\{100\}_{Al}$  and  $\{010\}_{Al}$  directions of the matrix according to the diffraction spots (Fig. 6i). Meanwhile, these



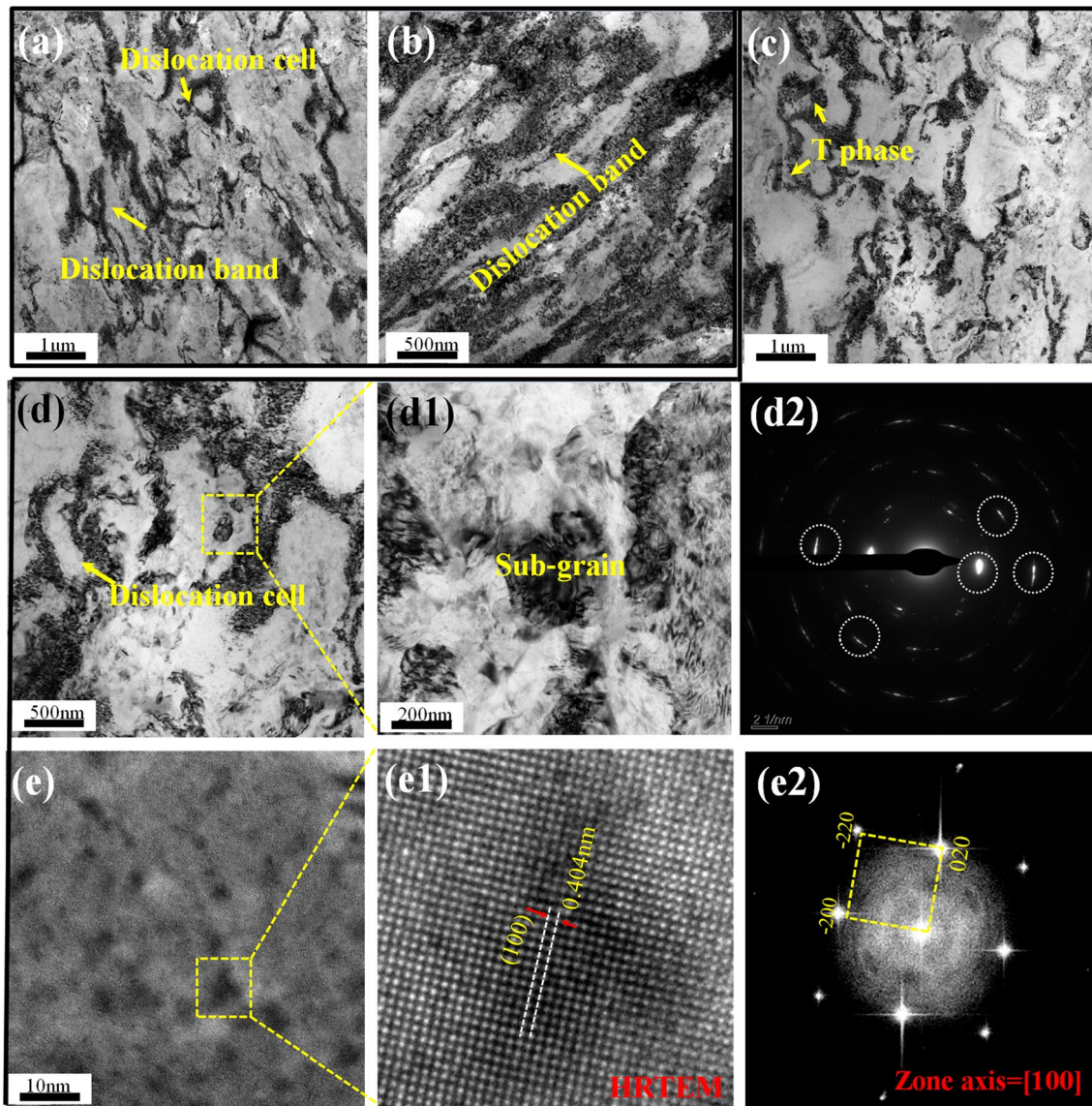


**Fig. 6** **a** TEM image of the CR sample; **b** the dislocation band in the CR sample; **c** TEM image of the WR sample; **d** dislocation cell in the WR sample; **d1** sub-grain in the WR sample; **d2** the diffraction spots

of WR sample; **e** high magnification of the WR sample; **e1** HRTEM image of **e** image; **e2** the diffraction spots of **e** image

diffraction spot features indicate that the precipitates mainly consist of the GP zone and  $\theta''$  phase.

The TEM images of the traditional peak-aging treatment T6 sample are also shown in Fig. 8 to further investigate the effect of thermomechanical treatment on the precipitation behavior of 211ZX alloy. Figures 8a, b show that numerous needle-like precipitates occurred in the T6 sample. The precipitates are confirmed to consist of the  $\theta'$  phase with a small amount of GP zone and  $\theta''$  phase according to the diffraction spots (Fig. 8d). The size of  $\theta'$  precipitates is measured to be approximately 100 nm long and 10 nm thick. The length of the GP zone is less than 10 nm, while the length of the  $\theta''$  phase is less than 30 nm. According to the orientation

relationship observed in the FFT diffractograms in Fig. 8d, the GP zone,  $\theta'$ , and  $\theta''$  precipitates grow along the [100] and [010] directions of the matrix. Additionally, the orientation relationships of  $\theta'$  and  $\theta''$  precipitates concerning the Al matrix can be identified as follows:  $\langle 100 \rangle \text{Al} // \langle 100 \rangle \theta'$  and  $\langle 100 \rangle \text{Al} // \langle 100 \rangle \theta''$ . The detailed precipitates information of the corresponding samples has been listed in Table 3.

### 3.3 XRD analysis

Figure 9a, b shows XRD patterns of the UA sample and CR sample with 50% and 70% reduction. The XRD profiles

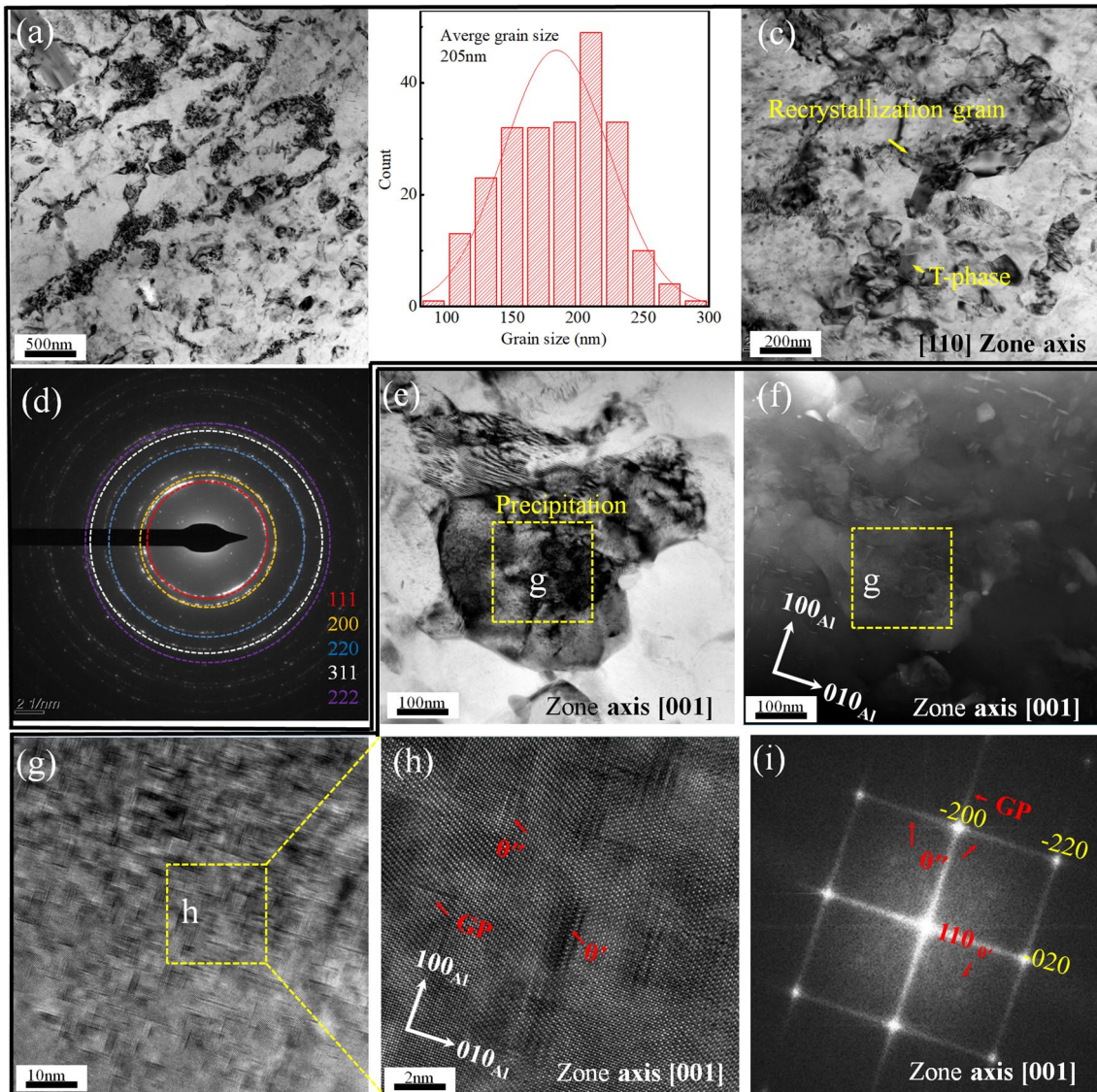


**Fig. 7** **a** TEM image of the WR-PA sample; **b** the grain size distribution of the WR-PA sample; **c** microstructure of the WR-PA sample along the [110] zone axis; **d** the diffraction spots of the WR-PA sample; **e** the UFG in WR-PA sample; **f** the HAADF-STEM image

of WR-PA sample **g** precipitate in the WR-PA sample; **h** HRTEM image of the precipitate in the nanocrystals; **i** the diffraction spots of **g** image

reveal the slight shifting of peaks from the standard positions to smaller Bragg angles, particularly for the CR sample with a 70% reduction. According to Bragg's law, the (220) interplanar spacing of the UA sample and CR samples with rolling reduction of 50% and 70% are calculated to be 4.0524 Å, 4.0584 Å, and 4.0624 Å, respectively, which are higher than the lattice constant of pure aluminum (4.04 Å). This indicates partial or complete dissolution of precipitates into the matrix and the introduction of lattice mismatch during CR. The result also suggests that increasing rolling reduction promotes the dissolution of precipitates. Figure 9c displays the XRD pattern of the CR, WR, and WR-PA samples. The trend of  $2\theta$  values

follows  $2\theta_{\text{CR-(220)}} < 2\theta_{\text{WR-(220)}} < 2\theta_{\text{WR-PA-(220)}}$ , which means that  $d_{\text{CR-(220)}} < d_{\text{WR-(220)}} < d_{\text{WR-PA-(220)}}$ . The results suggest that dissolution transformation occurs during the WR and PA processes. However, the XRD pattern shows that the diffraction peak of the precipitates does not appear in the CR and WR samples but rather in the 40°–45° range for WR-PA samples (Fig. 9d). The results suggest that the precipitate's reaction only occurs in the PA process, which was also confirmed by TEM observations.

The Williamson-Hall formula (1) is commonly used to calculate grain size ( $D$ ) and lattice microstrain ( $\epsilon$ ) in the deformed structure [27, 28].



**Fig. 8** **a** bright-field TEM images; **b** high magnification TEM image of the T6 sample; **c** HRTEM image of GP zone,  $\theta''$  phase and  $\theta'$  phase; **d** the corresponding diffraction spots of image **c**

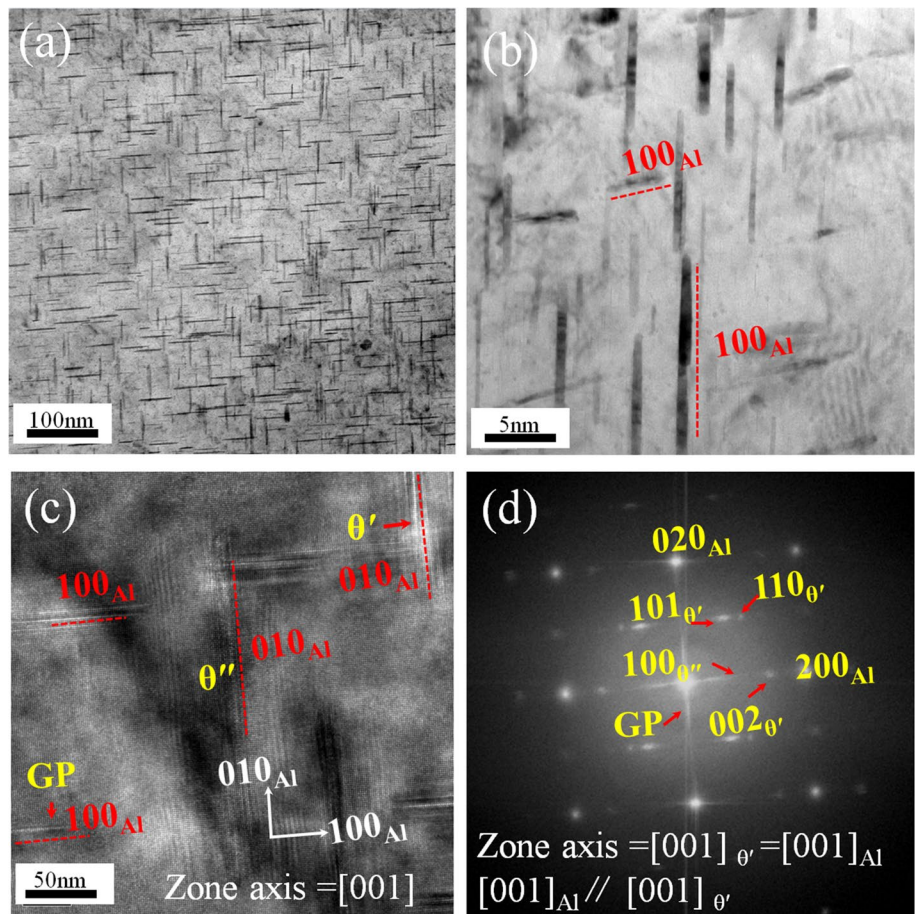
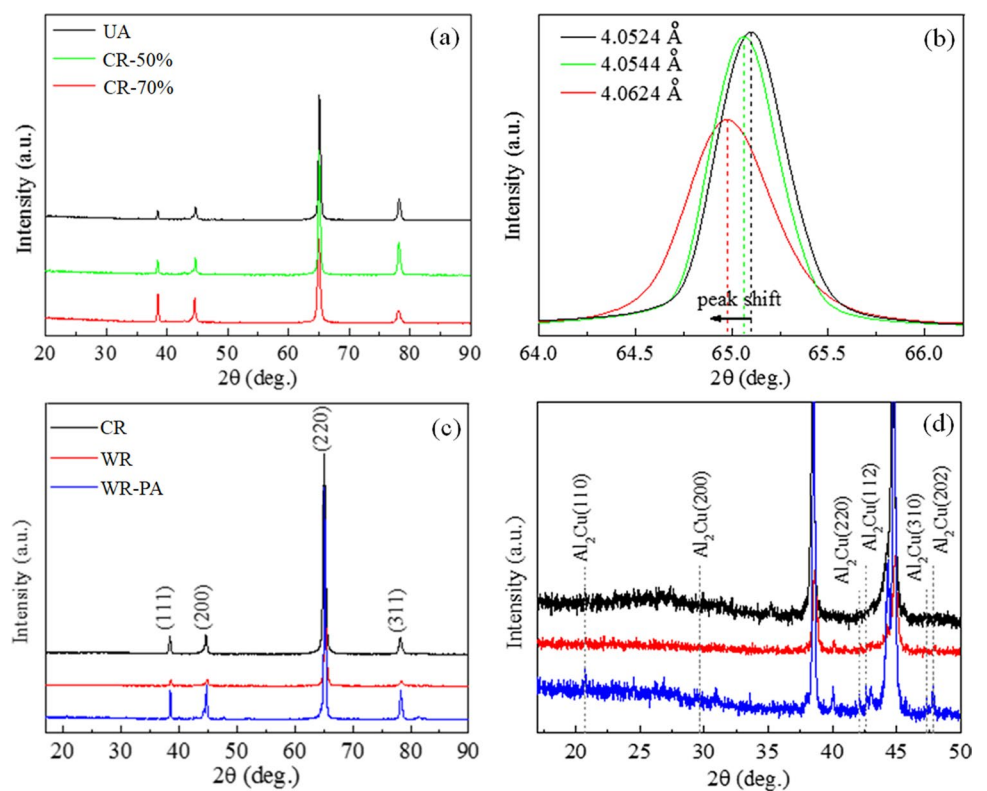


**Fig. 9** XRD pattern of the UA and CR samples: **a** fast scan; **b** slow scan; XRD pattern of the CR, WR, and WR-PA samples: **c** fast scan; **d** slow scan



$$B \cos \theta_B = \frac{K\lambda}{D} + \varepsilon \sin \theta_B \quad (1)$$

where  $B$  is the full width at half maximum (FWHM) and  $\theta_B$  is the Bragg angle,  $K$  is a constant ( $K=0.9$ ),  $\lambda$  is the wavelength of Cu radiation ( $\lambda=0.154$  nm),  $D$  is the grain size, and  $\varepsilon$  is the micro-strain. The values of  $D$  and  $\varepsilon$  can be obtained from the intercept and the slope of the fitted line after the linear fitting of  $B \cos \theta_B$  and  $\sin \theta_B$ . In addition, the dislocation densities are calculated as follows [27]:

$$\rho = \frac{2\sqrt{3}\varepsilon}{Db} \quad (2)$$

where  $\rho$  is the dislocation density and  $b$  represents the Burgess vector of aluminum alloy ( $b=0.286$  nm).

The results obtained from Eqs. (1) and (2) are shown in Fig. 10. As can be seen, the dislocation density in the CR sample is  $1.68 \times 10^{14} \text{ m}^{-2}$ . After WR processing, the dislocation density in the WR sample is slightly increased. This result indicates that a dynamic balance between dislocation annihilation and dislocation multiplication occurs during WR processing. In the subsequent peak aging, the dislocation density significantly decreases due to the annihilation of dislocations caused by precipitation and recrystallization.

The texture components affect the mechanical properties of alloys and can be quantitatively calculated by orientation distribution functions (ODFs) [36]. Face-centered cubic (fcc) metallic materials, brass, S, and copper textures commonly undergo cold rolling, and cube and Goss textures are normally formed by recrystallization. The exact positions of ideal textures in three ODF sections with a constant  $\varphi_2$  of  $0^\circ$ ,  $45^\circ$ , and  $65^\circ$  are displayed in Fig. 11a [37]. Figures 11b–d show the corresponding ODF sections of the UA, WR, and WR-PA samples, respectively. It can be found that they have different texture components. The texture is relatively weak for the UA sample.

On the other hand, the WR sample mainly consists of rolling texture, including Brass, copper, and S orientation. Moreover, Goss and cube textures can also be observed in the WR sample. The appearance of Goss and cube texture confirmed the occurrence of recrystallization. This also explains the reason for the formation of some ultrafine grains during WR. After peak aging, these textures remain up to the WR-PA sample, but the intensity of brass, copper, and S textures is slightly lower than the WR sample. The reason is that peak aging makes the rolling texture transform into a recrystallization texture. Some theories, such as the maximum energy release theory, micro-growth selection theory, and selection growth theory, were proposed to explain texture evolution during aging [37].

The volume fractions of different texture components at various samples were calculated, as indicated in Fig. 12. As shown in Fig. 12a, the volume fractions of brass, S, and copper textures in the UA sample are the lowest. The values are 5.83%, 5.42%, and 4.49%, respectively. After WR, the values of brass, S, and copper textures evidently increase to 33.76%, 11.53%, and 15.19%. This indicates that the deformation textures increased. Figure 12b displays the change of recrystallization texture. It is clear that the UA sample remains as the recrystallization texture from the as-received alloy, and the corresponding volume fractions are 5.25% and 6.13% for cube and Goss orientations. Compared to the UA sample, the recrystallization texture of the WR and WR-PA samples increases to 13.54% and 17.71%, respectively. Accordingly, the random texture volume fraction decreases gradually. The average Taylor factors can reflect the influence of texture on strength, which is related to the volume fraction of texture components in the alloy. Based on the texture results, the average Taylor factors of the UA, WR, and WR-PA samples can be calculated according to [38], and the results are shown in Fig. 12d.

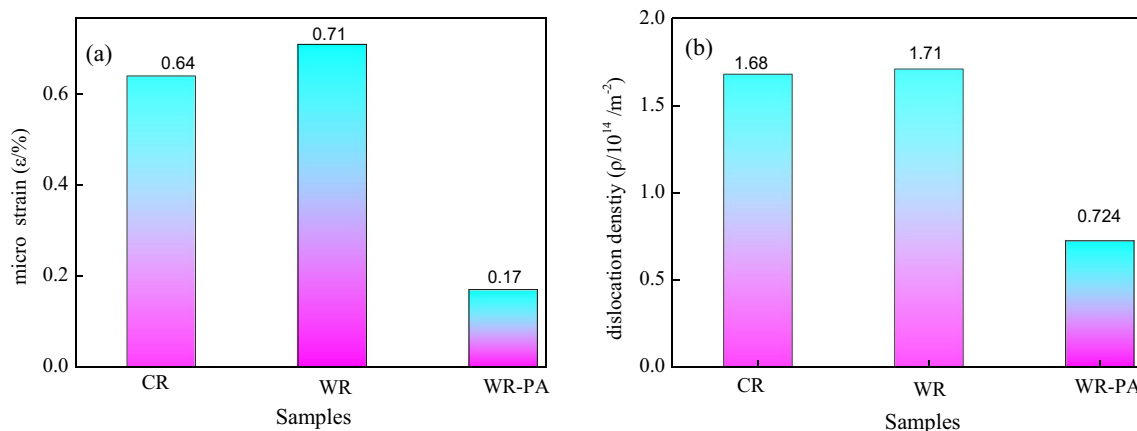


**Fig. 10** **a** Micro-strain and **b** dislocation density of the CR, WR, and WR- PA samples

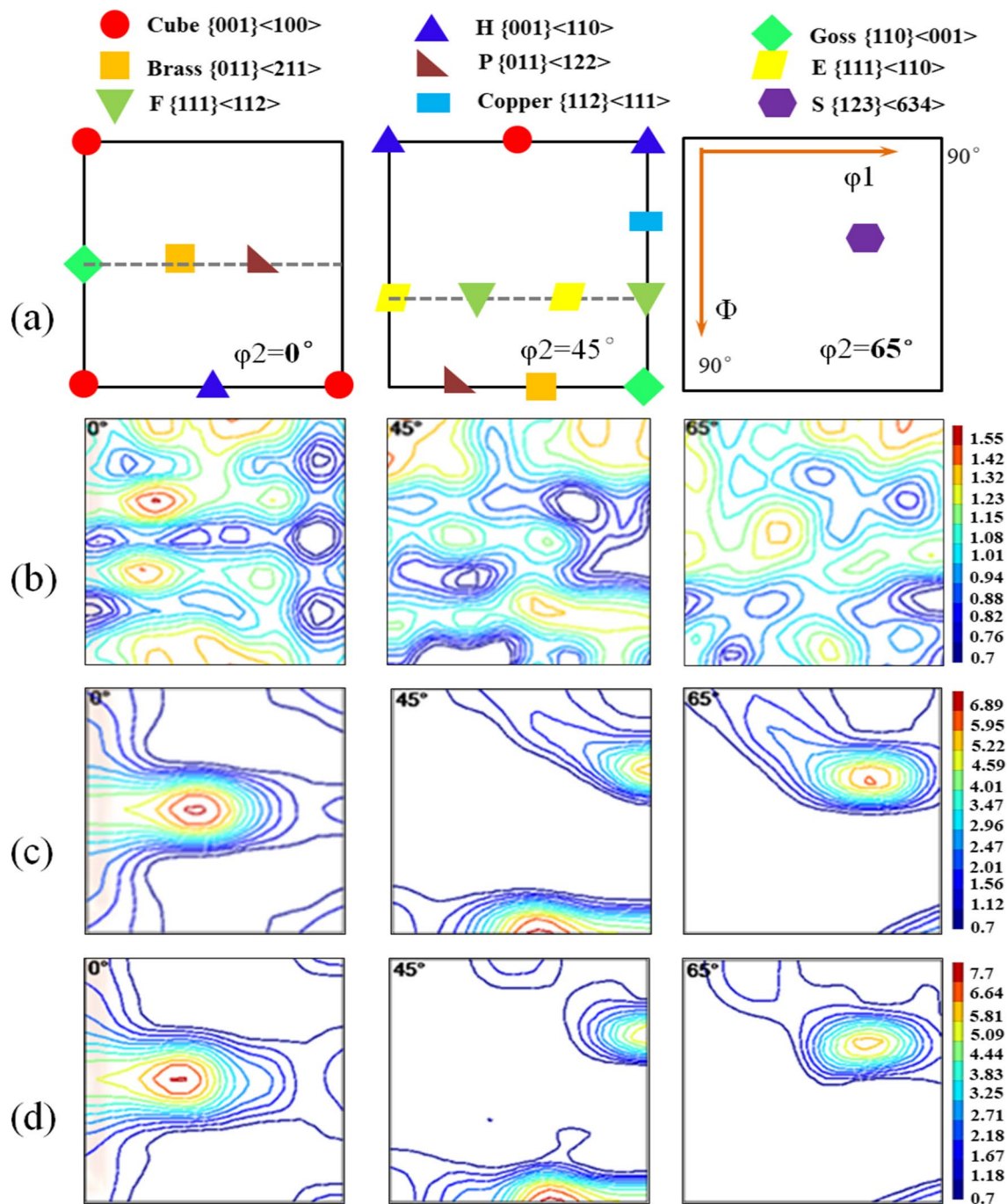


**Fig. 11** a Schematic drawing of section ( $\phi_2$  of  $0^\circ$ ,  $45^\circ$ , and  $65^\circ$ ) of ODF with typical texture components for FCC materials; ODFs ( $\phi_2$  of  $0^\circ$ ,  $45^\circ$ , and  $65^\circ$ ) of the different samples: b UA sample; c WR sample; d WR-PA sample

## 4 Discussion

### 4.1 Effect of TMT on precipitation behavior

The 211ZX aluminum alloy is a type of age-hardening aluminum alloy. The typical precipitation sequence can be described as follows: supersaturated solid solution  $\rightarrow$  GP

zones  $\rightarrow \theta'' \rightarrow \theta' \rightarrow \theta$ . The coherent GP zone and  $\theta''$  phase are regarded as the dominant strengthening phases at the peak-ageing condition [39]. However, SPD accelerates the precipitation kinetics and changes the precipitation sequence. The primary reason is that grain boundaries produced by SPD are characterized by relatively high energy, excess free volume, dislocation content, disordered atomic structure, and



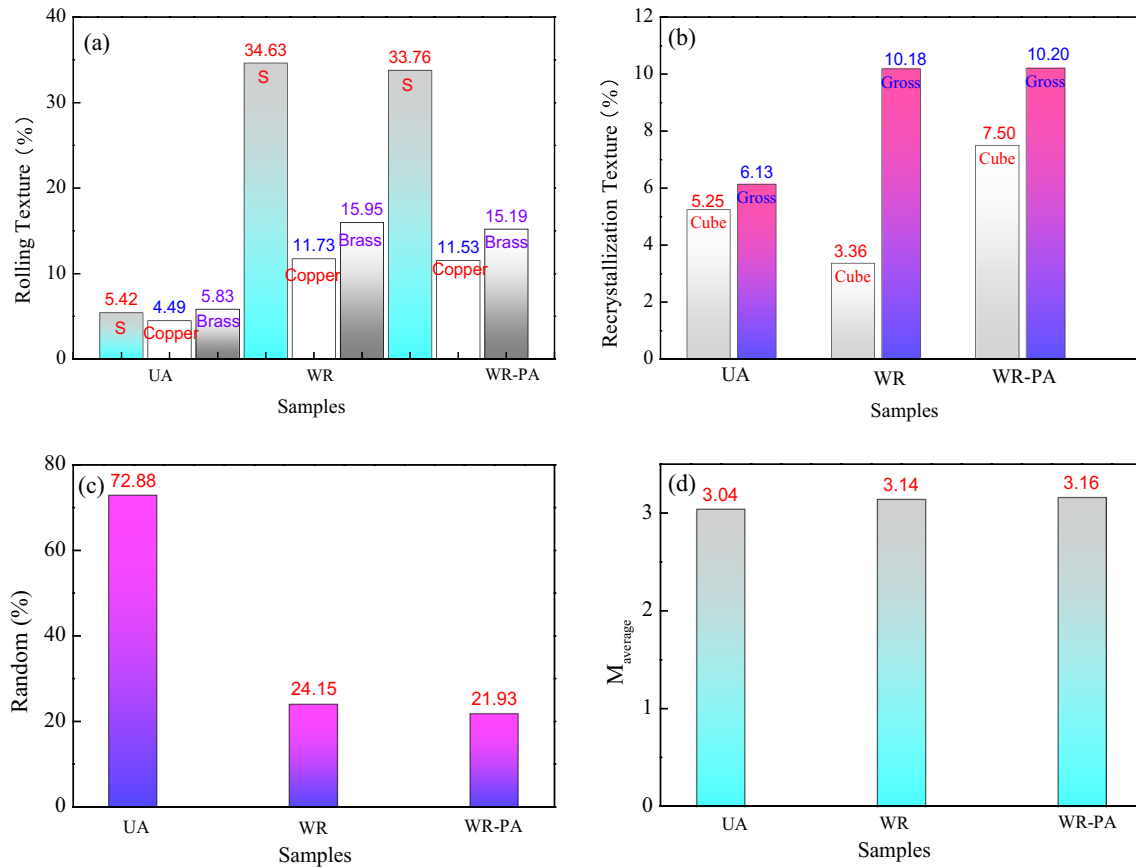


**Fig. 12** a, b, and c The volume fraction of the texture components (%) and d the average Taylor factors of the UA, WR, and WR-PA samples

energetically metastable state compared to their equilibrium counterpart. Therefore, incoherence precipitates with poor crystallographic match form directly at the grain boundaries to reduce high interfacial energy [40, 41]. On the other hand, these non-equilibrium grain boundaries act as fast diffusion paths for solute atoms and accelerate atomic diffusion and the segregation of solute atoms attached to the grain boundary. Accordingly, the chemical condition of the grain boundary precipitate can be easily satisfied.

In this work, HRTEM analysis confirms that the majority of the precipitates are located in the WR-PA sample matrix, and the GIPs phase mainly consists of the GP zone and  $\theta''$  phase, i.e., the same as with the T6 sample. Such

precipitate characteristics are attributed to the pre-existing precipitation and processing history of the 2112X aluminum alloy. First, CR can effectively suppress dynamic recovery and accumulate a higher density of dislocations. Consequently, high-density dislocations provide more nucleation sites for precipitations. Moreover, the high density of mobile dislocations effectively promotes the dissolution of pre-existing precipitation [42]. On the other hand, the ultra-low temperature can suppress the diffusion of dissolved solute, forming an enriched zone with Cu vacancies that serve as embryos of the GP zone during WR and subsequent aging [43]. Considering Cu diffusing in Al, the diffusion coefficient ( $D$ ) can be calculated by the following formula [44]:

$$D = D_0 \exp\left[-\frac{Q}{RT}\right] \tag{3}$$

where  $D_0$  is the pre-exponential coefficient that includes the jump frequency,  $Q$  is the activation energy,  $T$  is the temperature, and  $R$  is the gas constant ( $8.314 \text{ J}\cdot\text{mol}^{-1}\cdot\text{K}^{-1}$ ). The values for Cu bulk diffusion in a single Al crystal are  $D_0 = 6.47 \times 10^{-5} \text{ m}^2/\text{s}$  and  $Q = 135.1 \text{ kJ/mol}$  at 630–926 K.

**Table 3** Precipitates information of the corresponding samples

Sample	Precipitates
UA	GP Zone, $\theta''$ , $\theta'$ and T phase
CR	T phase
WR	T phase
WR-PA	GP Zone, $\theta''$ , $\theta'$ and T phase
T6	GP Zone, $\theta''$ , $\theta'$ and T phase

Extrapolation to 273 K (estimated cryogenic temperature) gives a value of  $D_{Cu} = 9.135 \times 10^{-31} \text{ m}^2/\text{s}$  [45]. Furthermore, the diffusion distance,  $x$ , diffusion coefficient,  $D$ , and time,  $t$ , can be described as follows:

$$x = \sqrt{Dt} \quad (4)$$

Assuming the diffusion distance is half of the average grain diameter (102.5 nm), diffusion from the interior of a grain to a grain boundary would take almost  $3.6 \times 10^6$  years. Dolgoplov et al. [46] calculated the  $Q$  and  $D_0$  values for Cu sub-grain boundary diffusion in polycrystalline Al as  $D_0 = 2 \text{ m}^2/\text{s}$  and  $Q = 118.5 \text{ kJ/mol}$ , respectively. Thus, a Cu atom diffusion length of 102.5 nm to a grain boundary at 273 K requires  $2 \times 10^4 \text{ s}$ . These calculations indicate that it is difficult for the dissolved solutes to undergo long-distance migration during the CR process. Previous investigations [47] have determined that the critical nucleation radius  $R_{Critical}$  of the precipitates is usually described by the following formula (5):

$$R_{Critical} = \frac{R_0}{\ln(C/C_{eq})}, \text{ and } R_0 = \frac{2\gamma V_{at}}{kT} \quad (5)$$

where  $k$  is the Boltzmann constant,  $T$  is the temperature,  $V_{at}$  is the atomic volume,  $C$  is the concentration of solute atoms in the solid solution,  $C_{eq}$  is the equilibrium concentration of solute atoms at temperature  $T$ , and  $\gamma$  is the interfacial energy when new phases are formed. Equation (5) indicates that a larger solid solubility  $C$  results in a smaller critical nucleation radius of the precipitation phase. Thus, when the pre-existing precipitates dissolve, CR increases the concentration of vacancies in the matrix and promotes solute segregation of Cu at matrix or intragranular dislocation. Alternatively, this process can form vacancy–solute complexes and clusters, allowing the relatively low concentration of solute to easily satisfy the chemical condition and form embryos in the matrix. The formation of embryos has been confirmed in the works of Xu and Liu et al. [23, 48, 49]. However, transforming the embryos to GIPs during cryogenic rolling is difficult. The driving force ( $\Delta G$ ) for the homogeneous nucleation of the GP zone is expressed by the following equation [47]:

$$\Delta G = -\frac{kT}{V_{at}} \ln\left(\frac{C}{C_{eq}}\right) \quad (6)$$

Moreover, the nucleation resistance ( $\Delta G^*$ ) of the GP zone can be expressed by the following equation [47]:

$$\Delta G^* = -\frac{16}{3} \pi \frac{V_{at}^2 \gamma^3}{k^2 T^2 \ln^2(C/C_{eq})} \quad (7)$$

When  $|\Delta G| > \Delta G^*$ , the GP zone starts to nucleate as follows:

$$\frac{kT}{V_{at}} \ln\left(\frac{C}{C_{eq}}\right) > \frac{16}{3} \pi \frac{V_{at}^2 \gamma^3}{k^2 T^2 \ln^2(C/C_{eq})} \quad (8)$$

$$T > \left(\frac{16}{3}\right)^{1/3} \frac{V_{at} \gamma}{k \ln(C/C_{eq})} \quad (9)$$

Equation (9) demonstrates that nucleation can occur only when the temperature is above a certain value to reach the nucleation activation energy of the GP region. Thus, a further process is designed to induce the transformation of clusters or embryos to GIPs. Considering low-temperature aging often weakens the age-hardening ability, the designed TMT process conducts a WR with a 60% reduction. Generally, short-time warm rolling provides the thermal driving force to promote uniform diffusion of solute atoms in the matrix, benefiting the composition concentration and uniform nucleation of the GP zone in the matrix [50, 51]. Experimental results also demonstrate that considerable large-sized GP zones appear in the matrix of the WR-PA samples, and only minor grain boundary precipitation is observed in Fig. 7f. Therefore, the designed TMT process produced composite nanostructures consisting of UFG and high-density GIPs in WR-PA samples.

Based on the above analysis, the schematic diagram of the microstructure evolution of 211ZX alloy during TMT processing is shown in Fig. 13. Comparing Figs. 13a, b, the UA sample produces many dislocations and vacancies after CR, and the GP region and  $\theta''$  phase dissolved. On the other hand, ultra-low temperature inhibits the long-range diffusion of solute atoms, and a zone enriched with Cu vacancies serves as the embryo of GIPs [23]. After warm rolling and subsequent peak aging (Figs. 13c, d), embryos are further transformed into GIPs.

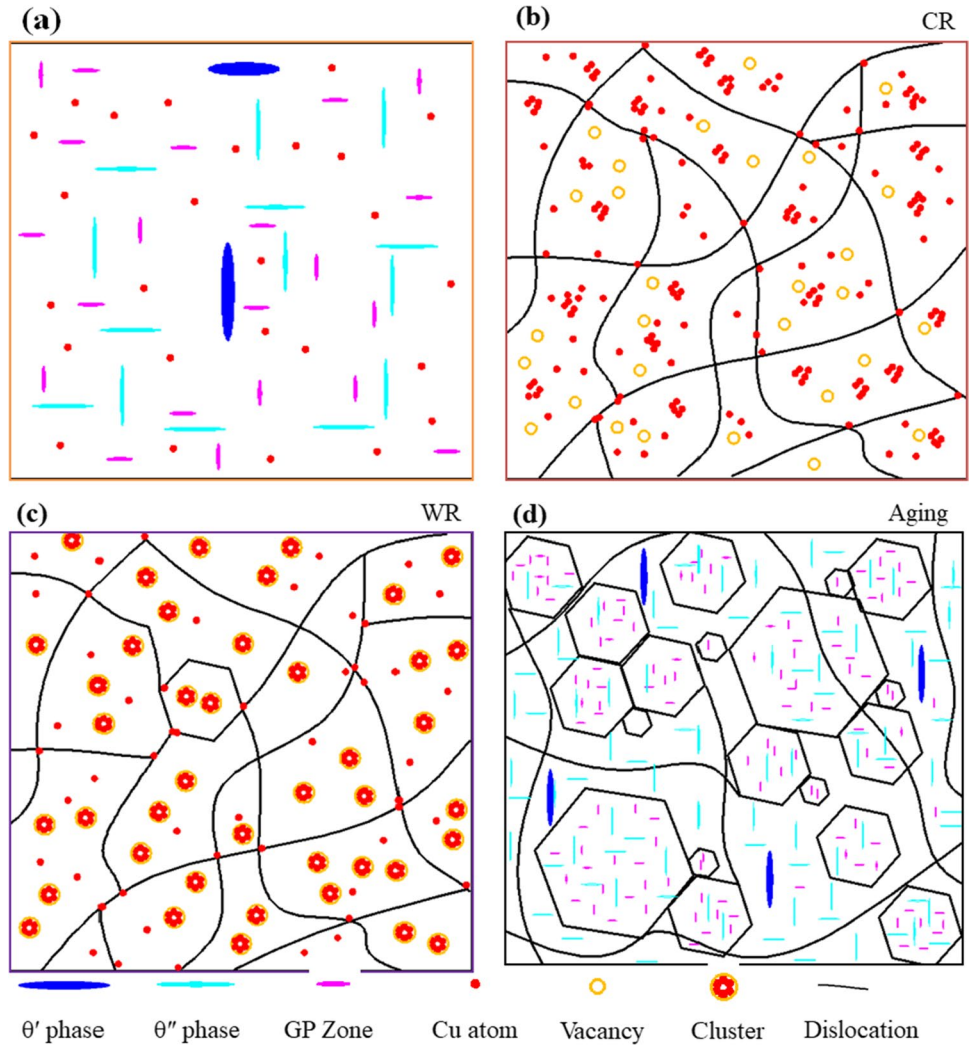
## 4.2 Mechanism of TMT processing on strength and plasticity

According to the tensile results, the TMT processing significantly improves the mechanical properties of the 211ZX aluminum alloy. The contributions of each strengthening mechanism in the T6 sample and the WR-PA sample are calculated to quantitatively characterize the influence of microstructure on yield strength after TMT processing. For age-hardening aluminum alloys, the yield strength is calculated according to Eq. (10) [27, 52]:

$$\sigma_y = \sigma_{gb} + M_{Average}(\tau_0 + \tau_s + \tau_p + \tau_d) \quad (10)$$

where  $\sigma_y$  is the yield strength,  $\sigma_{gb}$  is the contribution of grain boundary strengthening,  $\tau_0$  is the friction stress of approximately 10 MPa,  $\tau_s$  is the contribution of solid

**Fig. 13** Schematic illustrations of the precipitation evolution by following the present processing route: **a** under-aged treatment; **b** cryogenic rolling; **c** warm rolling; **d** peak aging



solution strengthening,  $\tau_d$  is the contribution of dislocation strengthening, and  $\tau_p$  is the contribution of precipitation strengthening.

The contribution of grain boundary strengthening ( $\sigma_{gb}$ ) is calculated according to the classical Hall–Petch formula:

$$\sigma_{gb} = kd^{-1/2} \tag{11}$$

where  $k$  is the Hall–Petch constant (0.10 MPa m<sup>1/2</sup> for aluminum alloys [53]), and  $d$  is the grain size. The average grain size of the T6 sample is 115 μm, while that of the WR-PA sample is only 205 nm. Accordingly, the  $\sigma_{gb}$  values for the T6 sample and the WR-PA sample are 11.19 MPa and 265.04 MPa, respectively.

The  $\tau_s$  and  $\tau_d$  components of the T6 sample are omitted, as all solution atoms are transformed into precipitated phases with low dislocation density after aging at 393 K for 24 h. Therefore, Eq. (10) for the T6 specimen can be simplified as follows:

$$\sigma_y = \sigma_{gb} + M_{Average}(\tau_0 + \tau_p) \tag{12}$$

The parameter  $\tau_p$  is governed by either the Orowan dislocation bypassing or dislocation shearing mechanisms, as a bypassing mechanism has a smaller strength increment, which is the operative mechanism [27, 53–55]. Simultaneously, Ye et al. [56] assert that all dislocations pass through the second phase via the bypass mechanism when the size of the second phase is 3–10 nm. Therefore, the calculations of  $\tau_p$  in this work are all conservative calculations that follow the Orowan mechanism. The corresponding formula is [54]:

$$\tau_p = \frac{0.4Gb \ln(2r/b)}{\lambda\pi(1-\nu)^{1/2}} \tag{13}$$

where  $b$  is the Burgers vector of 0.286 nm,  $\nu$  is the Poisson ratio of 0.33, and  $G$  is the shear modulus of 26.2 GPa. Furthermore,  $r$  and  $\lambda$  are the mean radius and spacing of the matrix precipitate, respectively. Parameter  $\lambda$  can be computed as  $\lambda = N^{-1/2}$ , where  $N$  represents the



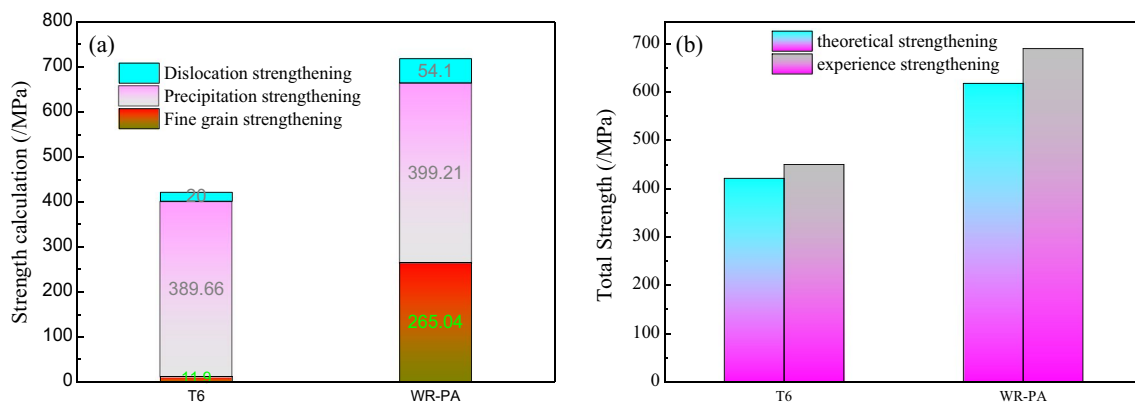


**Fig. 14** **a** The theoretical contributions of various strengthening mechanisms in the T6 and WR-PA samples; **b** theoretical and actual strengths in the WR-PA and T6 specimens

number density of matrix precipitates. The number density of precipitates  $N$  is calculated using the following formula:  $N = [(3n)/(1 + 0.8t)] \times A$ , where  $n$  is the measured number of precipitates in a field of view of the TEM sample,  $t$  is the thickness of the observed region, and  $A$  is the area of the field of view. For the non-spherical  $\theta'$  and  $\theta''$  precipitates, the radius of the precipitates can be replaced by the equivalent radius ( $r$ ). The average value of  $r$  can be calculated by the following equation:  $S = \pi \cdot r^2$  [55], where  $S$  represents the average cross-section area of the precipitates measured by thirty HRTEM images. The corresponding  $r$  and  $\lambda$  values of the T6 sample are calculated to be 6.83 nm and 35.2 nm, respectively, using this protocol.

The values of  $r$  and  $\lambda$  of the WR-PA samples calculated by the same method are 8.04 nm and 45.8 nm, respectively. Therefore, the value of  $\tau_p$  calculated by Eq. (13) is 399.21 MPa. Similarly, the contribution  $\tau_s$  of the WR-PA sample can also be neglected. The Bailey-Hirsch equation  $\tau_d = \alpha G b \rho^{1/2}$  is conducted to obtain  $\tau_d$ , where  $\alpha = 0.27$ ,  $\rho$  is the dislocation density, and  $G$  is the shear modulus of 26.2 GPa [57].

In addition, according to Eq. (10), the contributions of  $\tau_d$  and  $\tau_p$  also depend upon the Taylor factor. The research [50] has pointed out that the characteristic texture of peak aging samples is not altered compared to solution samples. Therefore,  $M_{Average}$  of T6 is the same as those of the UA sample. Thus, the values of  $M_{Average}$  in WR-PA and T6 are 3.14 and 3.04, respectively. The higher Taylor factor of the WR-PA sample has a greater impact on the strength improvement. According to Eq. (12), the value of  $\tau_p$  in the T6 sample is 389.66 MPa, whereas the values of  $\tau_p$  and  $\tau_d$  in the WR-PA sample are 399.21 MPa and 54.01 MPa, respectively. The theoretically calculated yield strengths of the T6 sample and the WR-PA sample are 400.8 MPa and 618.22 MPa, respectively.

Based on the above data, the contributions of various strengthening mechanisms in the T6 and the WR-PA samples are summarized in Fig. 14a. The higher yield strength of the WR-PA samples is primarily associated with the contribution of precipitation strengthening, grain refinement strengthening, and dislocation strengthening. In addition, the comparison between the experimental and theoretical results is also depicted in Fig. 14b. The presented theoretical results are in good agreement with the tensile results.

In this paper, the ductility of the WR-PA sample is significantly improved compared to the CR sample mainly due to two reasons. First, XRD results demonstrate that the dislocation density of the WR-PA sample is one order of magnitude lower than that of the CR sample (Fig. 10b), improving the work-hardening rate of the WR-PA sample. Second, TEM analysis in Fig. 7 shows that many GP zones and  $\theta''$  phases are formed in the WR-PA samples. The GP zone and  $\theta''$  phases with a coherent or semi-coherent interface relationship within the matrix lead to dislocation glide in the vicinity of the nano-precipitates, significantly improving the plasticity of the alloy [15].

## 5 Conclusions

In this work, a novel multi-step thermomechanical treatment (TMT) was designed to enhance the strength-ductility synergy of 211Z aluminum alloy. The effect of the multi-step TMT process on the microstructural evolution and mechanical properties was studied. The key findings of this research are summarized as follows:

- (1) The 211Z aluminum alloy prepared by the TMT process exhibited an excellent combination of strength and ductility. Quantitative calculations showed that the

high strength of the TMT-processed 211ZX aluminum alloy was attributed to a synergy effect of precipitation strengthening, fine grain strengthening, and dislocation strengthening. The improved plasticity was attributed to a decrease in dislocation density and a homogeneous distribution of coherent precipitates in the matrix.

- (2) The microstructure of the TMT-processed 211ZX aluminum alloy consists of UFG and homogeneously distributed GIPs, which are mainly composed of GP zone,  $\theta''$  phase, and a small amount of  $\theta'$  phase. This is the main reason for the excellent mechanical properties of the WR-PA sample. This TMT process provides a novel pathway for designing aluminum alloys with excellent mechanical properties.

**Acknowledgements** This work was financially supported by the Nature Science Foundation of GuiZhou province (ZK [2021054]), and the central government guides local science and technology development (Grant NO. [2019] 4011).

**Author contribution** TL: writing—original draft, investigation, formal analysis. MY: conceptualization, methodology, investigation, writing—review & editing, supervision, and funding acquisition. YJ: investigation, writing—review & editing. LL: methodology, writing—review & editing. KF: formal analysis.

**Data availability** Data will be available on request.

## Declarations

**Conflict of interest** The authors declare that they have no known competing financial interests or personal relationships that could have appeared to influence the work reported in this paper.

**Ethical approval** This study is approved by ethics committee of Guizhou University.

## References

- Belov NA, Akopyan TK, Shurkin PK, et al. Comparative analysis of structure evolution and thermal stability of commercial AA2219 and model Al-2wt.%Mn-2wt.%Cu cold rolled alloys. *J Alloy Compd.* 2021;864:158823.
- Li J, Lü S, Wu S, et al. Micro-mechanism of simultaneous improvement of strength and ductility of squeeze-cast Al-Cu alloy. *Mat Sci Eng A.* 2022;833:142538.
- Chen S, Li F, Chen K, et al. Synergic effect of hot deformation temperature and pre-straining on ageing precipitates and mechanical property of 2014 Al alloy. *Mater Charact.* 2020;167:110510.
- Snopiński P, Król M, Pagá M, et al. Effects of equal channel angular pressing and heat treatments on the microstructures and mechanical properties of selective laser melted and cast AlSi10Mg alloys. *Arch Civ Mech Eng.* 2021. <https://doi.org/10.1007/s43452-021-00246-y>.
- Damavandi E, Nourouzi S, Rabiee MS, et al. EBSD study of the microstructure and texture evolution in an Al-Si-Cu alloy processed by route A ECAP. *J Alloy Compd.* 2020;858:157651.
- Song D, Wang G, Zhou Z, et al. Developing a high-strength Al-11Si alloy with improved ductility by combining ECAP and cryorolling. *Mat Sci Eng A.* 2020;773:138880.
- Orlova TS, Latynina TA, Mavlyutov AM, et al. Effect of annealing on microstructure, strength and electrical conductivity of the pre-aged and HPT-processed Al-0.4Zr alloy. *J Alloy Compd.* 2019;784:41–8.
- Mathew RT, Singam S, Ghosh P, et al. The defining role of initial microstructure and processing temperature on microstructural evolution, hardness and tensile response of Al-Mg-Sc-Zr (AA5024) alloy processed by high pressure torsion. *J Alloy Compd.* 2022;901:163548.
- Jabłońska MB, Kowalczyk K, Tkocz M, et al. Dual rolls equal channel extrusion as unconventional SPD process of the ultralow-carbon steel: finite element simulation, experimental investigations, and microstructural analysis. *Arch Civ Mech Eng.* 2021;21:1.
- Kowalczyk K, Jabłońska MB, Tkocz M, et al. Effect of the number of passes on grain refinement, texture and properties of DC01 steel strip processed by the novel hybrid SPD method. *Arch Civil Mech Eng.* 2022;22(3):115.
- Liu G, Zhang GJ, Jiang F, et al. Nanostructured high-strength molybdenum alloys with unprecedented tensile ductility. *Nat Mater.* 2013;12:344–50.
- Shi J, Hou L, Zuo J, et al. Cryogenic rolling-enhanced mechanical properties and microstructural evolution of 5052 Al-Mg alloy. *Mat Sci Eng A.* 2017;701:274–84.
- Xu Z, Liu M, Jia Z, et al. Effect of cryorolling on microstructure and mechanical properties of a peak-aged AA6082 extrusion. *J Alloy Compd.* 2017;695:827–40.
- Panigrahi S, Jayaganthan K, Jayaganthan R. Development of ultrafine grained high strength age hardenable Al 7075 alloy by cryorolling. *Mater Design.* 2011;32:3150–60.
- Wen H, Topping TD, Isheim D, et al. Strengthening mechanisms in a high-strength bulk nanostructured Cu-Zn-Al alloy processed via cryomilling and spark plasma sintering. *Acta Mater.* 2013;61:2769–82.
- Xu PW, Luo HY, Li SJ, et al. Enhancing the ductility in the age-hardened aluminum alloy using a gradient nanostructured structure. *Mat Sci Eng A.* 2017;682:704–13.
- Khan MA, Wang Y, Malik A, et al. Microstructure characterization of 7055-T6, 6061-T6511 and 7A52-T6 Al alloys subjected to ballistic impact against heavy tungsten alloy projectile. *Arch Civ Mech Eng.* 2019;19:1484–1469.
- Khan MA, Xu CH, Hamza M, et al. Enhanced tensile strength in an Al-Zn-Mg-Cu alloy via engineering the precipitates along the grain boundaries. *J Mater Res Technol.* 2023;22:696–705.
- Khan MA, Wang Y, Afifi MA, et al. The formation of new (Al, Zn)3Zr precipitates in an Al-Zn-Mg-Cu aluminum alloy after aging treatment and their response to dynamic compression. *Arch Civ Mech Eng.* 2023;23:33.
- He G, Li K, Yang Y, et al. Effect of heat treatment on the microstructure and mechanical properties of cryogenic rolling 2195 Al-Cu-Li alloy. *Mater Sci Eng A.* 2021;822:141682.
- Dong F, Yi Y, Huang C, et al. Influence of cryogenic deformation on second-phase particles, grain structure, and mechanical properties of Al-Cu-Mn alloy. *J Alloy Compd.* 2020;827:154300.
- Mei L, Chen XP, Ren P, et al. Effect of warm deformation on precipitation and mechanical properties of a cryorolled Al-Zn-Mg-Cu sheet. *Mater Sci Eng A.* 2020;771:138608.
- Xu P, Luo H. Improving the ductility of nanostructured Al alloy using strongly textured nano-laminated structure combined with nano-precipitates. *Mat Sci Eng A.* 2016;675:323–37.
- Xiao R, Yang M, et al. Optimal design of 211ZX highstrength Aluminum alloy solid solution process based on response surface method. *Chin J Rare Met.* 2019;43:1040–6.

25. Gong QJ, Yang M, et al. Hot formability and dynamic recrystallization behavior of new high performance Aluminum alloy 211Z-X. *Chin J Rare Met.* 2018;42:36–44.
26. Zhang Z, Huang CW, et al. Effect of microstructure on high cycle fatigue behavior of 211Z.X-T6 Aluminum alloy. *Metals.* 2022. <https://doi.org/10.3390/met12030387>.
27. Ma K, Wen H, Tao H, et al. Mechanical behavior and strengthening mechanisms in ultrafine grain precipitation-strengthened aluminum alloy. *Acta Mater.* 2014;62:141–55.
28. Zhou W, Jiang C, Gan X, et al. Effect of shot peening on the microstructure of laser hardened 17–4PH. *Appl Surf Sci.* 2010;257:1154–60.
29. Shao CW, Zhang P, Zhu YK, et al. Simultaneous improvement of strength and plasticity: additional work-hardening from gradient microstructure. *Acta Mater.* 2018;145:413–28.
30. Feng K, Yang M, et al. The effect of a composite nanostructure on the mechanical properties of a novel Al-Cu-Mn alloy through multipass cold rolling and aging. *Appl Sci.* 2020;10:8109.
31. Zheng R, Sun Y, Ameyama K, et al. Optimizing the strength and ductility of spark plasma sintered Al 2024 alloy by conventional thermo-mechanical treatment. *Mat Sci Eng A.* 2014;590:147–52.
32. Gazizov M, Kaibyshev R. Effect of pre-straining on the aging behavior and mechanical properties of an Al-Cu-Mg-Ag alloy. *Mat Sci Eng A.* 2015;625:119–30.
33. Papazian JM. A calorimetric study of precipitation in aluminum alloy 2219. *Metall Trans A.* 1981;12:269–80.
34. Shen Z, Ding Q, Liu C, et al. Atomic-scale mechanism of the  $\theta'' \rightarrow \theta'$  phase transformation in Al-Cu alloys. *J Mater Sci Technol.* 2017;33:1159–64.
35. Liu MW, Zheng RX, Li J, et al. Achieving ultrahigh tensile strength of 1 GPa in a hierarchical nanostructured 2024 Al alloy. *Mater Sci Eng A.* 2020;788:139576.
36. Yang QY, Zhou YL, Tan YB, et al. Effects of microstructure, texture evolution and strengthening mechanisms on mechanical properties of 3003 aluminum alloy during cryogenic rolling. *J Alloy Compd.* 2021;884:161135.
37. Wang XF, Liu H, Tang XB, et al. Influence of asymmetric rolling on the microstructure, texture evolution and mechanical properties of Al-Mg-Si alloy. *Mater Sci Eng A.* 2022;844:143154.
38. Wang Z, Fang B, Zheng Z, et al. Improving the strength and ductility of Al-Mg-Si-Cu alloys by a novel thermo-mechanical treatment. *Mater Sci Eng A.* 2014;607:313–7.
39. Aniruddha B, Siegel DJ, et al. Precipitates in Al-Cu alloys revisited: atom-probe tomographic experiments and first-principles calculations of compositional evolution and interfacial segregation. *Acta Mater.* 2011;59:6187–204.
40. Deschamps A, Geuser FD, Horita Z, et al. Precipitation kinetics in a severely plastically deformed 7075 aluminium alloy. *Acta Mater.* 2014;66:105–17.
41. Hu T, Ma K, Topping TD, et al. Precipitation phenomena in an ultrafine-grained Al alloy. *Acta Mater.* 2013;61:2163–78.
42. Magalhaes DCC, Hupalo MF, Cintho OM. Natural aging behavior of AA7050 Al alloy after cryogenic rolling. *Mater Sci Eng A.* 2014;593:1–7.
43. Lechner W, Puff W, Mingler B, et al. Microstructure and vacancy-type defects in high-pressure torsion deformed Al-Cu-Mg-Mn alloy. *Scripta Mater.* 2009;61:383–6.
44. Wang SS, Jiang JT, Fan GH, et al. Accelerated precipitation and growth of phases in an Al-Zn-Mg-Cu alloy processed by surface abrasion. *Acta Mater.* 2017;131:233–45.
45. Peterson NL, Rothman SJ. Impurity diffusion in aluminum. *Phys Rev B.* 1970;8:3264–73.
46. Dolgoplov N, Rodin A, Simanov A, Gontar I. Cu diffusion along Al grain boundaries. *Mater Lett.* 2008;62:4477–9.
47. Deschamps A, Brechet Y. Influence of predeformation and ageing of an Al-Zn-Mg alloy-II. Modeling Precipitation Kinetics Yield Stress *Acta Mater.* 1998;47:293–305.
48. Li L, Jang JT, Cui XY, et al. Correlation between precipitates evolution and mechanical properties of Al-Sc-Zr alloy with Er additions. *J Mater Sci Technol.* 2022;99:61–72.
49. Liu CH, Li XL, Wang SH, et al. A tuning nano-precipitation approach for achieving enhanced strength and good ductility in Al alloys. *Mater Design.* 2014;54(2):144–8.
50. Jin T, Hai L, Hui J, et al. Enhanced mechanical properties of ARB-processed aluminum alloy 6061 sheets by subsequent asymmetric cryorolling and ageing. *Mater Sci Eng A.* 2016;674:256–61.
51. Kang UG, Lee JC, Jeong SW, Nam WJ. The improvement of strength and ductility in ultra-fine grained 5052 Al alloy by cryogenic- and warm-rolling. *J Mater Sci.* 2010;45:4739–44.
52. King H, Ha H, Lee J, et al. Outstanding mechanical properties of ultrafine-grained Al7075 alloys by high-pressure torsion. *Mater Sci Eng A.* 2021;810:141020.
53. Panigrahi SK, Jayaganthan R. Influence of solutes and second phase particles on work hardening behavior of Al 6063 alloy processed by cryorolling. *Mater Sci Eng A.* 2011;528:3147–60.
54. Wen H, Topping TD, Isheim D, et al. Strengthening mechanisms in a high-strength bulk nanostructured Cu-Zn-Al alloy processed via cryomilling and spark plasma sintering. *Acta Mater.* 2013;61:2769–82.
55. Hai L, Wei X, Wang Z, et al. Effects of re-ageing treatment on microstructure and tensile properties of solution treated and cold-rolled Al-Cu-Mg alloys. *Mater Sci Eng A.* 2016;650:254–63.
56. Ye L, Gang G, Zhang X, et al. Dynamic properties evaluation of 2519A aluminum alloy processed by interrupted aging. *Mater Sci Eng A.* 2014;590:97–100.
57. Yang MJ, Orekhov A, Hu ZY, et al. Shearing and rotation of  $\beta''$  and  $\beta$  precipitates in an Al-Mg-Si alloy under tensile deformation: In-situ and ex-situ studies. *Acta Mater.* 2021;220:117310.

**Publisher's Note** Springer Nature remains neutral with regard to jurisdictional claims in published maps and institutional affiliations.

Springer Nature or its licensor (e.g. a society or other partner) holds exclusive rights to this article under a publishing agreement with the author(s) or other rightsholder(s); author self-archiving of the accepted manuscript version of this article is solely governed by the terms of such publishing agreement and applicable law.